Interface cation migration kinetics induced oxygen release heterogeneity in layered lithium cathodes

Interface Cation Migration Kinetics Induced Oxygen Release Heterogeneity in Layered Lithium Cathodes

Chao-Fan Li[1,2#], Kangning Zhao[1,3#]*, Xiaobin Liao[1#], Zhi-Yi Hu[1,2]*, Lei Zhang[1], Yan Zhao[1], Sai Mu[4], Yanxi Li[5], Yu Li[1], Gustaaf Van Tendeloo[1,6], Congli Sun[1,2]*

[#]These authors contributed equally to this work

[1]State Key Laboratory of Advanced Technology for Materials Synthesis and Processing, International School of Materials Science and Engineering, Wuhan University of Technology, Wuhan 430070, China
[2]NRC (Nanostructure Research Centre), Wuhan University of Technology, Wuhan 430070, PR China
[3]Laboratory of Advanced Separations (LAS), École Polytechnique Fédérale de Lausanne (EPFL), Sion, Switzerland
[4]Materials Department, University of California, Santa Barbara, California 93106-5050, USA
[5]Department of Materials Science and Engineering, Stanford University, Stanford, CA 94305, USA
[6]EMAT (Electron Microscopy for Materials Science), University of Antwerp, Antwerp B-2020, Belgium

*corresponding authors: conglisun@whut.edu.cn, zhiyi.hu@whut.edu.cn, kangning.zhao@epfl.ch.

ABSTRACT: The irreversible release of the lattice oxygen in layered cathodes is one of the major degradation mechanisms of lithium ion batteries, which accounts for a number of battery failures including the voltage/capacity fade, loss of cation ions and detachment of the primary particles, *etc*. Oxygen release is generally attributed to the stepwise thermodynamic controlled phase transitions from the layered to spinel and rock salt phases. Here, we report a strong kinetic effect from the mobility of cation ions, whose migration barrier can be significantly modulated by the phase epitaxy at the degrading interface. It ends up with a clear oxygen release heterogeneity and completely different reaction pathways between the thin and thick areas, as well as the interparticle valence boundaries, both of which widely exist in the mainstream cathode design with the secondary agglomerates. This work unveils the origin of the heterogenous oxygen release in the layered cathodes. It also sheds light on the rational design of cathode materials with enhanced oxygen stability by suppressing the cation migration.

KEYWORDS: *in situ* STEM, lithium ion batteries, layered lithium transition metal oxides, oxygen release, local heterogeneity

Rechargeable lithium ion batteries (LIBs) are dominating today's portable electronic devices. They keep attracting great research interest in the continuous improvement of their specific energy, cycling stability and operation safety for high-energy-density applications like electric vehicles.[1–4] Cathode materials are the major limiting factor for improving energy density, in which the lithium transition metal oxide (LTMO) cathodes are the most promising candidates but only slightly more than half of the theoretical capacities is achieved.[5–10] On the other hand, the oxygen release issue of LTMO is responsible for a lot of failures including voltage/capacity fading,[11,12] loss of cation ions,[13] intergranular cracking and detachment of primary particles.[12,14–20] Improving energy density makes the oxygen release issue more critical as thermal runaway can be triggered through the reaction of released oxygen with the flammable electrolyte.[21] The oxygen release is generally understood by the thermodynamic driven phase transitions that lower the cation valence, leaving under-coordinated oxygen that eventually results in the formation of O_2 molecules. However, the fundamental mechanism is still far from clear, since the oxygen release can happen far below the phase transition threshold.

Here, we use $LiCoO_2$ (LCO) to demonstrate the oxygen release mechanism as LCO is the protype structure for the LTMO cathodes. LCO is still the mainstream commercial cathode for its high energy density, excellent cyclability, and rate performance.[22,23] Various studies have been conducted on the oxygen release mechanisms of layered cathodes. Wu et al. compared different types of layered cathodes and reported the rapid growth of rock salt shells as the general oxygen release pathway of overcharged cathodes.[24] Hwang et al. found the thermally induced

decomposition of Ni rich layered cathodes at temperatures below 100 °C with surface pores and strong particle-to-particle variation.[25] They also investigated the effect of different ratios of transition metals on the oxygen release issues.[26] Karki et al. found the strong environment effect on the oxygen release susceptibility,[27] which is further applied by Sharifi-Asl et al. who used atomically thin layer of reduced graphene oxide to trap the released lattice oxygen that significantly enhanced the thermal stability.[21] Xu et al. and Gu et al. reported the detailed mechanisms of transition metal ions migration leading to phase transitions and oxygen release at the surface of layered cathodes.[28,29] Recent studies of the oxygen release mechanism of LCO by Sharifi-Asl et al. and Sun et al. showed a strong facet anisotropy, vacancy dependence and surface effect.[13,30] Oxygen release was also found to be responsible for intergranular cracking.[14,31] The surface effect was also widely reported in stability studies of various LTMOs, in which the capacity/voltage fading, structure degradation, phase evolution and capacity loss are always severe at the edge.[24,28,30,32–36] This raises a major question as what drives the phase transitions and why the dynamics is always faster at the edge. On the other hand, the early stage of the phase transition involves the migration of Co, which is kinetically trapped due to the strong octahedral preference of CoO_6.[37] The dynamic migration barrier of Co ions plays a critical role to initiate the early phase transition that is beyond the control of the thermodynamic driving forces. As such, the global equilibrium phase diagram no longer works while the local mobility of Co migration will trigger a consecutive phase evolution with strong local heterogeneity. Understanding the thermal instability mechanism and the local heterogeneity remains a challenge and is of great significance.

In this work, the thermally induced phase transition of LCO cathode crystals was directly observed by *in-situ* heating inside an aberration corrected scanning transmission electron

microscopy (STEM). A phase evolution mechanism involving the initial defect assisted Co migration, companied by a strong topotactic phase growth with intense competition between the layered and the spinel phases is revealed. This gives rise to different degradation pathways and onset temperatures between the thin edges and the thicker inner areas. Thermodynamics overrides the migration kinetics when the temperature reaches ~400 °C. The Co ions get enough mobility with abrupt phase transitions, generating holes that completely changes the surface morphology. Interparticle variation is also studied, in which the oxygen diffusion driven by the concentration gradient plays a critical role at elevated temperatures. This reduces the migration barrier of Co by breaking the CoO_6 octahedra framework, which causes an early phase degradation at much lower temperatures.

RESULTS AND DISCUSSION

The morphology of the LCO cathode is shown by the scanning electron microscopy (SEM) top down image in Fig. 1a and the annular bright field (ABF) STEM cross section image in Fig. 1b. The LCO is densely packed with a grain size ranging from several hundred nanometers to ~3 μm. The general crystal structure is determined by X-ray diffraction in Fig. 1c, which matches well with the $LiCoO_2$ pattern (JCPDS no. 016-0427) and shows a perfect α-$NaFeO_2$ layered structure with $R\bar{3}m$ space group. The LCO sample is clearly textured, indicating a preferential growth along the [001] direction. It should be noted that, in order to increase the sample consistency among different characterizations, the diffraction was conducted using the same sample mounted on the *in situ* TEM chip based focused ion beam (FIB) stage. Due to the limited loading mass and orientations for LCO on the chip based stage, the diffraction peaks are not strong. The typical atomic structure can also be directly observed in the following high

resolution STEM images. The dense packing of LCO micrometer-sized crystals provides a higher volumetric and areal energy density and reduced electrode/electrolyte contact area, which has been widely used in electronic devices. The typical electrochemical performance is shown in Fig. 1d and the commercialized $LiCoO_2$ delivers a very stable cycling performance with no capacity decay at 100 mA g^{-1}. The charge and discharge curves in Fig. 1e overlap quite well with no obvious voltage decay. Surface STEM images and dQ/dV curves (Fig. S1 in supporting materials) also suggest no anion redox reaction in potential range of 3-4.2 V.

Fig. 2a shows a low magnification high angle annular dark field (HAADF) STEM image of a FIB mounted LCO cathode on a *DENSsolution* heating chip. The TEM sample targets LCO particles along the sharp edges, which gives rise to the [100] oriented columnar grains that allows a direct visualization of the individual Co and Li layers. Three areas are studied in detail, namely, the thin edge area (yellow ellipse), the thick center area (red circle), and the interparticle boundary (blue arrow), as highlighted in Fig. 2a. Both the edge and center area show the bulk structure of LCO at room temperature (Fig. 1S and Fig. 2c), while the neighboring grain below the blue arrow presents a clear particle-to-particle valence deviation and shows a lower valance state of Co. A detailed structure analysis of the STEM images and the electron energy loss spectroscopy (EELS) data will be presented in Fig. 6.

Fig. 2b are low magnification HAADF-STEM images that shows a general thermal behavior of the thick center area. No visible changes of the surface morphology can be found at temperatures below 200 °C, while a clear particle nucleation appears from 200 to 400 °C. Above 400 °C, a sharp morphology transition is observed with the fast formation of holes. Zone axis electron diffraction patterns (ZAP) as a function of temperature are provided in Fig. S2 in the supporting materials. With increasing temperatures, no significant difference of the ZAP can be

found for temperatures as high as 400 ℃, which generally matches with the previous reports.[26,30]

Fig. 2c shows the corresponding high magnification HAADF-STEM images. Each image is taken 30 min after reaching the set temperature. Room temperature (20 ℃) LCO in Fig. 2c shows the typical layered R$\bar{3}$m phase, in which the CoO_6 and LiO_6 octahedra layers are stacked alternatively. The HAADF signal is proportional to Z^a with a ranging from 1.6 -1.9. The image is dominated by high-Z Co cation layers and the LiO_6 layers are invisible. It is therefore interesting that additional contrast can be found at the position of the Li layers at temperatures as low as 150 ℃ (Fig. 2c), which reveals the cross-layer migration of the Co ions into the Li layers. Fig. 2e shows the intensity line profile along the red and green arrows indicated in the 150 ℃ STEM image in Fig. 2c. The decreasing Co layer intensity is correlated with the increasing Li layer intensity. A slight intensity shift along the channel layer is also observed (black arrow in Fig. 2e), which indicates a Co diffusion within the Li layers after the initial cross-layer migration. This agrees with previous results that show a highly reduced migration barrier of the transition metal ions in the Li layers.[38,39] The cross-layer migration is widely observed in various lithium transition metal oxides, which is generally recognized as the onset of the spinel phase transition.[28,30,34,36,40,41] We will denote the structure with Co cross-layer migration as "intermediate spinel (IS)", since it has not yet developed into a complete spinel structure. A more complete spinel phase can be observed and will be discussed later in the edge and boundary area. When the temperature reaches 200 ℃, a particle like surface nucleation starts to show up. Because of the smooth pristine surface created by FIB fine polishing, the surface nucleation increases the local thickness; this is directly observed as a brighter contrast in the HAADF-STEM images. It is not surprising that the surface nucleation initiates on top of the IS phase,

which is believed to be defect assisted. This can be directly observed from Fig. 2c at 250 °C as the local IS phase becomes brighter due to the increasing thickness affected by surface nucleation and growth. Most of the surface nucleation particles showing up at 250 °C (Fig. 2b) contain clear Co migration to the Li layer (more images can be found in Fig. S3). The corresponding intensity line profile is shown in Fig. 2f, in which the Co intensity clearly increases compared with the Co intensity in Fig. 2e.

Interestingly, at temperatures below 400 °C, phase degradation does not follow a linear pathway with increasing surface nucleation and temperature, *i.e.*, the IS phase does not develop into the complete Co_3O_4-type spinel phase with increasing temperatures below 400 °C. In fact, some of the Co can even migrate back to the Co layer to retain the bulk-like LCO structure, as shown by the 350 °C HAADF-STEM image in Fig. 2c. The surface nucleation shows a mixture of IS and bulk-like phases at a temperature of 350 °C. This indicates a layered-IS phase competition that is beyond the general thermodynamic driving force. Detailed Competition observed at a lower magnification, as well as within a single surface particle can be found in Fig. S4. Above 400 °C, the IS phase starts to dominate, as shown in the 400 °C image in Fig. 2c and the corresponding intensity line profile in Fig. 2g. When the temperature reaches 450 - 500 °C, a dramatic phase transition happens with the abrupt surface growth at the expense of neighboring LCO, resulting in the formation of holes. The 500 °C-2 in Fig. 2c is taken after staying an additional 30 min at 500 °C, which shows a more complete phase transition to the widely reported rock salt (RS) phase.[26,27,30,32,36,37] The corresponding intensity line profile is given in Fig. 2h.

EELS was performed to understand the temperature-dependent electronic structure of the LCO cathode. Area averaged O-K edges at 20 °C, 200 °C, 350 °C, 400 °C and 450 °C and the

local O-K edges on the surface nucleation (particle P1 at 200 °C and P2 at 350 °C) are shown in Fig. 2d. All the spectra are background subtracted using a power law method and the plural scattering is removed by Fourier-ratio deconvolution. The O-K edge is the excitation from oxygen 1s to 2p orbitals above the Fermi level. The resulting spectrum can be interpreted in a first-order approximation as the unoccupied oxygen p projected density of states in the presence of a core hole. Although oxygen 2p orbitals are fully occupied in a complete ionic model, the hybridization between oxygen 2p and Co 3d and 4sp states reduces the number of filled O 2p states. Charge transfer occurs between the unfilled Co orbitals and oxygen 2p states, which creates O 2p holes. This makes the O-K edge sensitive to the filling of Co 3d orbitals, which has been widely used as the indication of valence states,[27] oxygen vacancies[42] and even spin states[40]. The O-K edge can thus be divided into two regions. The first region directly at the threshold is the oxygen 2p weight in the states of Co 3d character, which is often referred as the prepeak in transition metal oxides. In Fig. 2d, the oxygen prepeak is at about 532 eV. The second region, ~11 eV above the threshold, is attributed to oxygen 2p states hybridized with Co 4s and 4p states. The O2pCo4sp peaks in Fig. 2d are aligned and normalized. The lower intensity of the prepeak is related to an increasing Co 3d occupancy (reduction of Co ions).

The O-K edge of the pristine LCO shows a strong prepeak. With increasing temperature, the prepeak shows no clear drop for temperatures up to 350 °C. A clear prepeak drop starts around 400 °C, which reveals the significant amount of oxygen vacancies in the layered structure. The inset in Fig. 2d is the EEL spectrum guide image and mapping of the oxygen area density, which shows a clear oxygen poor feature of the well-developed surface nucleation. The local O-K edges on the surface nucleation (P1) present a clear prepeak drop at a temperature as low as 200 °C, which is a strong evidence of early Co migration assisted by oxygen vacancies. It

is notable that oxygen vacancies still exist after the Co migration back to its original transition metal layers at 350 ℃ (P2), which indicates the irreversible process of the oxygen release. The layered R$\bar{3}$m phase can sustain with a significant amount of oxygen vacancies, but it is difficult for an oxygen vacancy to re-trap molecular O_2 from the back migration of the Co ions. Further temperature increase to 400 ℃ will accumulate enough oxygen vacancies and trigger a dramatic phase transition from the IS phase to the RS phase. A clear phase boundary of the layered structure and the RS structure can be seen from Fig. 2c at 450 ℃. The intensity of the O-K prepeak in EELS also decreases dramatically with a significant oxygen release.

The thermal degradation of LCO can be understood as an oxygen vacancy assisted Co migration followed by a topotactic phase transition (epitaxial growth of degrading phases directly on top of the Co migration region). Sharifi-Asl and co-authors have reported the pioneer work on the oxygen release heterogeneity in LCO which reveals a strong dependence on the facet orientation.[30] In order to consider the structure orientation, the same *in situ* heating experiment is also performed on LCO with a different orientation (Fig. S4), where the topotactic transition with a strong phase epitaxy can also be observed with a weak orientation dependence. This reveals that the epitaxial phase degradation is more likely to originate from the metal oxygen octahedra framework shared among the initial phase transitions. Facet anisotropy is less significant in flat surfaces. The epitaxial order exists for temperatures up to 450 ℃ (Fig. S2). The diffraction spots of the degrading phases have a strong epitaxial relation with the ones of the initial phase until the dramatic thermodynamic driven phase degradation takes place.

The phase transition is completely different at the edge. As shown in Fig. 3a-b, a dendritic phase propagation is observed at the edge which is in sharp contrast with the particle-like surface nucleation at the center area. The dendritic phase appears at a temperature lower than

the onset temperature of the surface nucleation (Fig. S6). The growth pathway is also significantly different. The phase evolution in the center area can be viewed as a spontaneous particle nucleation that slightly increases its size with increasing temperature, while a spreading growth mode of the dendrite with a clear reaction front dominates at the edge. Fig. 3d shows the reaction front of the dendrite phase, in which the layered, spinel and RS phase can be simultaneously viewed.[34,36] Fig. 3e-g are the corresponding magnified images with the structure model superimposed. Since the layered to spinel and further to the RS phase transition is associated with the decreasing lattice oxygen content, the growth of the dendrite phase is also an oxygen release pathway, accompanied with an increasing ratio of Co on the dendrite phase, as evidenced by the energy dispersive X-ray spectroscopy (EDS) quantification mapping (Fig. 3c inset). It is worth noting that the valence of Co decreases with the reducing lattice oxygen, which can be deduced from the EELS data in Fig. S7.

It is widely reported that the thermal degradation of LCO involves a series of phase transitions from the layered $R\bar{3}m$ phase to the spinel $Fd\bar{3}m$ phase and further to the RS $Fm\bar{3}m$ phase with increasing temperature.[26,30,32,37] While the global phase evolution in Fig. 2 generally follows this transition pathway, our results indicate a strong local heterogeneity that is much more complicated than the simple thermodynamic phase picture. The layered to spinel transition starts with the Co migration to the Li layer. This is kinetically controlled due to the strong CoO_6 octahedra preference, which means that Co can be trapped at the octahedra center even though the thermodynamic driving force for phase transition exists.[37] As shown in Fig. 2c and Fig. 2d, although oxygen loss can start very early at local areas that induces the onset of the spinel transition, a more significant and continuous oxygen loss is initiated with the sustained and irreversible cross layer migration of Co ions. This is due to the transition metal-oxygen

octahedra trapping, in which more significant phase transition requires the breaking of the octahedra framework. In this way, the cation and oxygen tend to reinforce each other to alleviate any possible degradation that could compromise the octahedra integrity. Creating Li vacancies will lower the energy barrier for the migration of Co. This is generally observed as the charged LCO undergoes the spinel transition at much lower temperatures.[26,27,30,32] The formation of oxygen vacancies, as shown in Fig. 2d on the local surface nucleation particles also reduces the migration barrier since it directly alters the CoO_6 ligand field,[38,39] which distorts the Co off the CoO_6 center and reduces its migration barrier to the adjacent Li layer. Our recent report quantitatively correlated the number of Co oxygen vacancy neighbors with the reducing migration barrier, which shows that oxygen vacancies significantly facilitate the phase degradation.[13] With the formation of the IS phase assisted by oxygen vacancies, surface nucleation keeps growing, preferably on top of the IS phase (Fig. 2c and Fig. S3). However, a further temperature rise to below 400 ℃ does not dramatically enrich the ratio of the spinel phase. In fact, for the center region, as shown in Fig 2, the IS phase is trapped and unable to develop into the complete spinel observed in Fig. 3d and Fig. 3f at the edge region. On the other hand, it is interesting that the IS phase competes with the layered phase, indicating a strong structure order imposed by the pristine LCO lattice. The IS phase trapping and the competition with the pristine layered phase ceases at temperatures above 400 ℃. The thermodynamic driving force overrides the kinetic force (trapping) plus the structure order imposed by the host LCO. With increasing Co mobility gained from the thermal energy, a dramatic phase transition happens that directly drives the IS phase into the RS phase, without developing into a complete spinel since the spinel phase is thermodynamically unstable at temperatures above 400 ℃.[43] The

surface morphology is also significantly altered, creating holes that are widely observed in previous reports.[27,30,32]

In the edge area, the epitaxial phase evolution ends up with a different picture. As the LCO is much thinner at the edge (the thickness of the edge is about 30 nm while the center region is around 100 nm, as determined from the low-loss EELS), the weight of the IS phase can quickly dominate at elevated temperatures. Our previous report also showed that the fast Co surface migration will facilitate the phase degradation,[13] which can be responsible for the low degradation onset temperature due to the short ion migration length in the thin edge area. On the other hand, the epitaxy is known as a mutual interaction between the host and growth materials,[44] which means that the epitaxially degraded phase will also impose a structure order to the host LCO. In this case, it can be understood as an additional coulomb repulsive force to Co ions at the bulk/IS degrading interface. The migration of Co ions at the bulk/IS interface is calculated by density functional theory (DFT) using the climbing image nudged elastic band (CI-NEB) method. The diffusion barrier of the interface Co to a Li vacancy is calculated as a function of the number of migrated Co in the adjacent IS phase, as shown in Fig. 4. A linear decreasing of the migration barrier can be observed with increasing number of the Co migration in the IS phase. It should be noted that Li could also stay at the neighboring tetrahedral site, forming an intermediate Li dumbbell instead of creating a Li vacancy with the migration of Co ions to occupy the Li site.[3] The same CI-NEB calculation is performed to consider the potential Li dumbbell configuration, which is shown in Fig. S8. Interestingly, the diffusion barrier of Co in the adjacent layered phase is negative with the Li dumbbell configuration. Although the direct visualization of Li dynamics is difficult, both Li configurations indicate that the development of the epitaxial IS phase will facilitate the phase degradation of the adjacent

layered phase. With the robust development of the IS phase to a threshold, the top IS phase will convert the thin LCO host into the IS phase, instead of the long-term competition. At last, the oxygen vacancy concentration also plays a critical role. The concentration gradient induced oxygen vacancy diffusion will become significant at elevated temperatures, which is important in the catalytic activity, oxygen ion conductivity and electrochemical properties.[45] The diffusion of oxygen vacancies could alleviate the local accumulation of vacancies on the surface nucleation, which mitigates the local phase degradation in the thicker center region. However, the thinner edge has limited oxygen diffusion pathways, as well as insufficient bulk support to accept oxygen vacancies. As a result, the ion migration triggers the consecutive phase transitions to spinel and RS phase at a much lower temperature. The short surface ion migration length also ends up with faster transition dynamics. The degrading phase quickly develops its own edges and grows by attracting material from the surface migration. It results in a more significant surface effect with an additional growth direction by surface spreading, which can be observed in Fig. 3. In fact, the observation of a reduced decomposition onset temperature with higher amount of mass loss was reported by using nano-sized LCO which has a higher edge exposing.[46] However, this is the first time that the complete atomic origin is unveiled. The Co local migration, surface nucleation, epitaxial growth and phase competition is schematically presented in Fig. 5.

In addition to the edge, a unique thermal behavior can also be observed at the interparticle boundary with different valence states. Fig. 6a is a low angle annular dark field (LAADF) STEM image at 350 °C of a grain boundary between the center area and a neighboring grain. The LAADF signal is sensitive to the strain field, which clearly emphasizes the significant phase transition at the boundary. The bottom grain has a lower oxidation state, as can be

demonstrated by O-K edge EELS, while the upper grain is the pristine LCO that is stable at 400 °C as shown in Fig. 2. Such a particle to particle variation of lithium transition metal oxides is widely reported due to the stress anisotropy in the sintered polycrystalline aggregate and differential expansion within a single particle.[25,47]

A clear phase variation in the vicinity of the boundary is evident in Fig. 6d. The layered phase is still present away from the boundary, but it gradually turns into the spinel and finally the RS phase with decreasing distance to the boundary. The corresponding EELS signals are plotted in Fig. 6e, which shows an increasing oxygen release and reduction of Co close to the boundary. The HAADF-STEM of area 1 and 2 do not present a clear difference while their O-K prepeak shows a clear drop in area 2. It reveals an accumulation of oxygen vacancies prior to the spinel phase transition. The oxygen release is driven by the concentration gradient between LCO crystals with different valence states. Oxygen vacancies diffuse across the boundary, and the Co ions get a higher mobility and will jump out of the CoO_6 trap more easily with increasing oxygen vacancies (inset in Fig 6e.).[13] The phase degradation apparently takes place as a function of distance from the boundary, with the growth of the RS phase at the expense of spinel and the layered phases. The boundary spinel phase completely transforms to RS at a much lower temperature of 350 °C, as shown in Fig. 6b-d.

CONCLUSIONS

In situ STEM analysis has demonstrated the atomic origin of the heterogenous thermal degradation pathways of the LCO cathode, which is due to a complicated interplay of the cross-layer migration barrier of Co ions, the shared metal-oxygen framework among the early phase degradation and the edge space confinement effect. The limited mobility of Co in the CoO_6

framework plays a critical role in the low temperature thermal behavior, which introduces a kinetic stability that slows down the early phase degradation. The kinetic control can be compromised by introducing oxygen vacancies. The edge, with limited space to mitigate the vacancy accumulation, has a lower degradation onset temperature. The shared oxygen-metal framework results in a topotactic phase transition that imposes an epitaxial structure order at the degrading interfaces, which also contributes to the different thermal properties between the thin and thick areas. Our results provide an atomic insight into the heterogeneous degradation pathways, which also indicate the potential structure instability when preparing nanostructured LCO cathodes. Valence homogeneity is also critical as the particle to particle valence variation will introduce an additional boundary degradation pathway.

METHODS

The LiCoO$_2$ sample. LTMOs usually consist of primary particles assembled into large secondary particles to increase the energy density and reduce the exposed surface.[14,48] Commercially available close packed LiCoO$_2$ secondary particles were used.

STEM characterization. The thermal behavior was investigated in real time using a Thermo Fisher Themis transmission electron microscope equipped with aberration correctors for the probe forming lens and the imaging lens, operated at 300 KV. The probe has a convergence semi angle of 17.8 mrad with beam current about ~30 pA. Under these conditions the estimated probe is less than 1 Å. Electron energy loss spectroscopy (EELS) was performed on a Gatan Quantum 965 GIF system. Dual EELS data were obtained with a spectrometer dispersion chosen for simultaneous visualization of both zero-loss and core-loss (O K and Co L edges). The energy resolution determined by full-width at half-maximum of the zero-loss peak was ~1.2 eV. The

background was subtracted using the power law method, with plural scattering removed by Fourier-ratio deconvolution. Samples are only exposed to electron beam when taking images or spectra. Live observation was not performed in order to reduce the possible beam damage. The phase transition can be confirmed to be temperature driven, since extended electron beam exposing at room temperature does not introduce any phase degradation.

STEM Sample preparation and *in-situ* heating. Samples for *in situ* heating were transferred by a standard focused ion beam (FIB) (Thermo Fisher Helios Nanolab G3) process[49] and mounted onto the *DENSsolution* heating chip. The final polishing voltage was reduced to 2 kV with a low tilt angle to reduce ion damage and increase the thickness difference between edge and central areas.

Density functional theory (DFT) calculations. DFT calculations were performed using the VASP (Vienna Ab-initio Simulation Package), with Perdew-Burke-Ernzerhof (PBE) generalized gradient approximation (GGA) + U (3.91 eV) method to correct the electronic correlation among the Co 3d orbitals. The climbing image nudged elastic band (CI-NEB) method was carried out for the diffusion simulation of Co atom, following the sample procedure used in our previous publication.[13]

ASSOCIATED CONTENT:

Supporting information

S1. STEM images of the edge LCO and the dQ/dV curve.
S2. Zone axis electron diffraction pattern of the thick area as a function of temperature.
S3. Phase transition induced early surface nucleation.
S4. The back migration of Co.
S5. The weak facet dependence.
S6. The evolution of the edge dendrite phase.

S7. The decreasing Co valence following the spreading front of the dendrite phase.
S8. Li dumbbell configuration

AUTHOR INFORMATION

Corresponding authors

* Email: conglisun@whut.edu.cn, zhiyi.hu@whut.edu.cn, kangning.zhao@epfl.ch

ORCID

Zhi-Yi Hu: 0000-0003-1371-8778

Kangning Zhao: 0000-0003-2916-4386

Xiaobin Liao: 0000-0002-2455-832X

Yan Zhao: 0000-0002-1234-4455

Congli Sun: 0000-0001-8132-272X

AUTHOR CONTRIBUTION

C.S and K.Z conceived the project. C.S, C.L, and Z.H performed the *in situ* STEM experiment and interpretation. X.L and Y.Z conducted the DFT simulations. K.Z conducted the XRD, the battery measurement and data interpretation. All the authors contributed to the discussions and the writing of the manuscript.

ACKNOWLEDGEMENTS

Materials Synthesis and Processing, and the State Key Laboratory of Silicate Materials for Architectures (all of the laboratories are at Wuhan University of Technology).

REFERENCES

[1]   Q. Liu, X. Su, D. Lei, Y. Qin, J. Wen, F. Guo, Y.A. Wu, Y. Rong, R. Kou, X. Xiao, F. Aguesse, J. Bareño, Y. Ren, W. Lu, Y. Li, Approaching the capacity limit of lithium cobalt oxide in lithium ion batteries via lanthanum and aluminium doping, Nat. Energy. 3 (2018) 936–943.

[2]   X. Dai, A. Zhou, J. Xu, Y. Lu, L. Wang, C. Fan, J. Li, Extending the High-Voltage Capacity of LiCoO2 Cathode by Direct Coating of the Composite Electrode with Li_2CO_3 via Magnetron Sputtering, J. Phys. Chem. C. 120 (2016) 422–430.

[3]   S. Hy, H. Liu, M. Zhang, D. Qian, B.-J. Hwang, Y.S. Meng, Performance and design considerations for lithium excess layered oxide positive electrode materials for lithium ion batteries, Energy Environ. Sci. 9 (2016) 1931–1954.

[4]   S. Jiao, X. Ren, R. Cao, M.H. Engelhard, Y. Liu, D. Hu, D. Mei, J. Zheng, W. Zhao, Q. Li, N. Liu, B.D. Adams, C. Ma, J. Liu, J.-G. Zhang, W. Xu, Stable cycling of high-voltage lithium metal batteries in ether electrolytes, Nat. Energy. 3 (2018) 739–746.

[5]   S. Li, Z. Jiang, J. Han, Z. Xu, C. Wang, H. Huang, C. Yu, S.-J. Lee, P. Pianetta, H. Ohldag, J. Qiu, J.-S. Lee, F. Lin, K. Zhao, Y. Liu, Mutual modulation between surface chemistry and bulk microstructure within secondary particles of nickel-rich layered oxides, Nat. Commun. 11 (2020) 4433.

[6]   W. Li, E.M. Erickson, A. Manthiram, High-nickel layered oxide cathodes for lithium-based automotive batteries, Nat. Energy. 5 (2020) 26–34.

[7]   D.-S. Ko, J.-H. Park, B.Y. Yu, D. Ahn, K. Kim, H.N. Han, W.S. Jeon, C. Jung, A. Manthiram, Degradation of High-Nickel-Layered Oxide Cathodes from Surface to Bulk: A Comprehensive Structural, Chemical, and Electrical Analysis, Adv. Energy Mater. 10 (2020) 2001035.

[8]   G. Assat, S.L. Glazier, C. Delacourt, J.-M. Tarascon, Probing the thermal effects of voltage hysteresis in anionic redox-based lithium-rich cathodes using isothermal calorimetry, Nat. Energy. 4 (2019) 647–656.

[9]   G.-L. Xu, Q. Liu, K.K.S. Lau, Y. Liu, X. Liu, H. Gao, X. Zhou, M. Zhuang, Y. Ren, J. Li, M. Shao, M. Ouyang, F. Pan, Z. Chen, K. Amine, G. Chen, Building ultraconformal protective layers on both secondary and primary particles of layered lithium transition metal oxide cathodes, Nat. Energy. 4 (2019) 484–494.

[10]   P. Yan, J. Zheng, J. Liu, B. Wang, X. Cheng, Y. Zhang, X. Sun, C. Wang, J.-G. Zhang, Tailoring grain boundary structures and chemistry of Ni-rich layered cathodes for enhanced cycle stability of lithium-ion batteries, Nat. Energy. 3 (2018) 600–605.

[11]   E. Hu, X. Yu, R. Lin, X. Bi, J. Lu, S. Bak, K.-W. Nam, H.L. Xin, C. Jaye, D.A. Fischer, K. Amine, X.-Q. Yang, Evolution of redox couples in Li- and Mn-rich cathode materials and mitigation of voltage fade by reducing oxygen release, Nat. Energy. 3 (2018) 690–698.

[12]   H. Liu, M. Wolf, K. Karki, Y.-S. Yu, E.A. Stach, J. Cabana, K.W. Chapman, P.J. Chupas, Intergranular Cracking as a Major Cause of Long-Term Capacity Fading of Layered Cathodes, Nano Lett. 17 (2017) 3452–3457.

[13]   C. Sun, X. Liao, F. Xia, Y. Zhao, L. Zhang, S. Mu, S. Shi, Y. Li, H. Peng, G. Van Tendeloo, K. Zhao, J. Wu, High-Voltage Cycling Induced Thermal Vulnerability in $LiCoO_2$ Cathode: Cation Loss and Oxygen Release Driven by Oxygen Vacancy Migration,

ACS Nano. 14 (2020) 6181–6190.

[14] L. Mu, R. Lin, R. Xu, L. Han, S. Xia, D. Sokaras, J.D. Steiner, T.-C. Weng, D. Nordlund, M.M. Doeff, Y. Liu, K. Zhao, H.L. Xin, F. Lin, Oxygen Release Induced Chemomechanical Breakdown of Layered Cathode Materials, Nano Lett. 18 (2018) 3241–3249.

[15] S. Nadimpalli, D. Abraham, Stress Evolution in Lithium-Ion Composite Electrodes during Electrochemical Cycling and Resulting Internal Pressures on the Cell Casing, J. Electrochem. Soc. 162 (2015) A2656.

[16] D.J. Miller, C. Proff, J.G. Wen, D.P. Abraham, J. Bareño, Observation of Microstructural Evolution in Li Battery Cathode Oxide Particles by In Situ Electron Microscopy, Adv. Energy Mater. 3 (2013) 1098–1103.

[17] E.-J. Lee, Z. Chen, H.-J. Noh, S.C. Nam, S. Kang, D.H. Kim, K. Amine, Y.-K. Sun, Development of Microstrain in Aged Lithium Transition Metal Oxides, Nano Lett. 14 (2014) 4873–4880.

[18] A. Mukhopadhyay, B.W. Sheldon, Deformation and stress in electrode materials for Li-ion batteries, Prog. Mater. Sci. 63 (2014) 58–116.

[19] N. Kızıltaş-Yavuz, M. Herklotz, A.M. Hashem, H.M. Abuzeid, B. Schwarz, H. Ehrenberg, A. Mauger, C.M. Julien, Synthesis, structural, magnetic and electrochemical properties of $LiNi_{1/3}Mn_{1/3}Co_{1/3}O_2$ prepared by a sol–gel method using table sugar as chelating agent, Electrochim. Acta. 113 (2013) 313–321.

[20] R. Robert, P. Novák, Structural Changes and Microstrain Generated on $LiNi_{0.8}0Co_{0.15}Al_{0.05}O_2$during Cycling: Effects on the Electrochemical Performance, J. Electrochem. Soc. 162 (2015) A1823–A1828.

[21] S. Sharifi-Asl, F.A. Soto, T. Foroozan, M. Asadi, Y. Yuan, R. Deivanayagam, R. Rojaee, B. Song, X. Bi, K. Amine, J. Lu, A. Salehi-khojin, P.B. Balbuena, R. Shahbazian-Yassar, Anti-Oxygen Leaking $LiCoO_2$, Adv. Funct. Mater. 29 (2019) 1901110.

[22] K. Mizushima, P.C. Jones, P.J. Wiseman, J.B. Goodenough, Li_xCoO_2 (0<x<-1): A new cathode material for batteries of high energy density, Mater. Res. Bull. 15 (1980) 783–789.

[23] M.S. Whittingham, Lithium Batteries and Cathode Materials, Chem. Rev. 104 (2004) 4271–4302.

[24] L. Wu, K.-W. Nam, X. Wang, Y. Zhou, J.-C. Zheng, X.-Q. Yang, Y. Zhu, Structural Origin of Overcharge-Induced Thermal Instability of Ni-Containing Layered-Cathodes for High-Energy-Density Lithium Batteries, Chem. Mater. 23 (2011) 3953–3960.

[25] S. Hwang, S.M. Kim, S.-M. Bak, B.-W. Cho, K.Y. Chung, J.Y. Lee, W. Chang, E.A. Stach, Investigating Local Degradation and Thermal Stability of Charged Nickel-Based Cathode Materials through Real-Time Electron Microscopy, ACS Appl. Mater. Interfaces. 6 (2014) 15140–15147.

[26] S. Hwang, S.M. Kim, S.-M. Bak, S.Y. Kim, B.-W. Cho, K.Y. Chung, J.Y. Lee, E.A. Stach, W. Chang, Using Real-Time Electron Microscopy To Explore the Effects of Transition-Metal Composition on the Local Thermal Stability in Charged $Li_xNi_yMnzCo_{1−y–z}O_2$ Cathode Materials, Chem. Mater. 27 (2015) 3927–3935.

[27] K. Karki, Y. Huang, S. Hwang, A.D. Gamalski, M.S. Whittingham, G. Zhou, E.A. Stach, Tuning the Activity of Oxygen in $LiNi_{0.8}Co_{0.15}Al_{0.05}O_2$ Battery Electrodes, ACS Appl. Mater. Interfaces. 8 (2016) 27762–27771.

[28] B. Xu, C.R. Fell, M. Chi, Y.S. Meng, Identifying surface structural changes in layered Li-excess nickel manganese oxides in high voltage lithium ion batteries: A joint experimental

and theoretical study, Energy Environ. Sci. 4 (2011) 2223–2233.

[29]   M. Gu, I. Belharouak, J. Zheng, H. Wu, J. Xiao, A. Genc, K. Amine, S. Thevuthasan, D.R. Baer, J.-G. Zhang, N.D. Browning, J. Liu, C. Wang, Formation of the Spinel Phase in the Layered Composite Cathode Used in Li-Ion Batteries, ACS Nano. 7 (2013) 760–767.

[30]   S. Sharifi-Asl, F.A. Soto, A. Nie, Y. Yuan, H. Asayesh-Ardakani, T. Foroozan, V. Yurkiv, B. Song, F. Mashayek, R.F. Klie, K. Amine, J. Lu, P.B. Balbuena, R. Shahbazian-Yassar, Facet-Dependent Thermal Instability in $LiCoO_2$, Nano Lett. 17 (2017) 2165–2171.

[31]   P. Yan, J. Zheng, T. Chen, L. Luo, Y. Jiang, K. Wang, M. Sui, J.-G. Zhang, S. Zhang, C. Wang, Coupling of electrochemically triggered thermal and mechanical effects to aggravate failure in a layered cathode, Nat. Commun. 9 (2018) 2437.

[32]   S. Hwang, Y. Lee, E. Jo, K.Y. Chung, W. Choi, S.M. Kim, W. Chang, Investigation of Thermal Stability of P2–Na_xCoO_2 Cathode Materials for Sodium Ion Batteries Using Real-Time Electron Microscopy, ACS Appl. Mater. Interfaces. 9 (2017) 18883–18888.

[33]   Q. Li, Z. Yao, E. Lee, Y. Xu, M.M. Thackeray, C. Wolverton, V.P. Dravid, J. Wu, Dynamic imaging of crystalline defects in lithium-manganese oxide electrodes during electrochemical activation to high voltage, Nat. Commun. 10 (2019) 1692.

[34]   L. Ben, H. Yu, B. Chen, Y. Chen, Y. Gong, X. Yang, L. Gu, X. Huang, Unusual Spinel-to-Layered Transformation in $LiMn_2O_4$ Cathode Explained by Electrochemical and Thermal Stability Investigation, ACS Appl. Mater. Interfaces. 9 (2017) 35463–35475.

[35]   A. Tornheim, S. Sharifi-Asl, J.C. Garcia, J. Bareño, H. Iddir, R. Shahbazian-Yassar, Z. Zhang, Effect of electrolyte composition on rock salt surface degradation in NMC cathodes during high-voltage potentiostatic holds, Nano Energy. 55 (2019) 216–225.

[36]   H. Tan, S. Takeuchi, K.K. Bharathi, I. Takeuchi, L.A. Bendersky, Microscopy Study of

Structural Evolution in Epitaxial $LiCoO_2$ Positive Electrode Films during Electrochemical Cycling, ACS Appl. Mater. Interfaces. 8 (2016) 6727–6735.

[37] L. Wang, T. Maxisch, G. Ceder, A First-Principles Approach to Studying the Thermal Stability of Oxide Cathode Materials, Chem. Mater. 19 (2007) 543–552.

[38] P. Yan, J. Zheng, Z.-K. Tang, A. Devaraj, G. Chen, K. Amine, J.-G. Zhang, L.-M. Liu, C. Wang, Injection of oxygen vacancies in the bulk lattice of layered cathodes, Nat. Nanotechnol. 14 (2019) 602–608.

[39] M. Gu, I. Belharouak, A. Genc, Z. Wang, D. Wang, K. Amine, F. Gao, G. Zhou, S. Thevuthasan, D.R. Baer, J.-G. Zhang, N.D. Browning, J. Liu, C. Wang, Conflicting Roles of Nickel in Controlling Cathode Performance in Lithium Ion Batteries, Nano Lett. 12 (2012) 5186–5191.

[40] R.F. Klie, J.C. Zheng, Y. Zhu, M. Varela, J. Wu, C. Leighton, Direct Measurement of the Low-Temperature Spin-State Transition in $LaCoO_3$, Phys. Rev. Lett. 99 (2007) 47203.

[41] R. Gu, Z. Ma, T. Cheng, Y. Lyu, A. Nie, B. Guo, Improved Electrochemical Performances of $LiCoO_2$ at Elevated Voltage and Temperature with an In Situ Formed Spinel Coating Layer, ACS Appl. Mater. Interfaces. 10 (2018) 31271–31279.

[42] D.A. Muller, N. Nakagawa, A. Ohtomo, J.L. Grazul, H.Y. Hwang, Atomic-scale imaging of nanoengineered oxygen vacancy profiles in $SrTiO_3$, Nature. 430 (2004) 657–661.

[43] S. Sharifi-Asl, J. Lu, K. Amine, R. Shahbazian-Yassar, Oxygen Release Degradation in Li-Ion Battery Cathode Materials: Mechanisms and Mitigating Approaches, Adv. Energy Mater. 9 (2019) 1900551.

[44] K. Yan, L. Fu, H. Peng, Z. Liu, Designed CVD growth of graphene via process engineering, Acc. Chem. Res. 46 (2013) 2263–2274.

[45] Y. Ding, Y. Choi, Y. Chen, K.C. Pradel, M. Liu, Z.L. Wang, Quantitative nanoscale tracking of oxygen vacancy diffusion inside single ceria grains by in situ transmission electron microscopy, Mater. Today. (2020).

[46] J. Geder, H.E. Hoster, A. Jossen, J. Garche, D.Y.W. Yu, Impact of active material surface area on thermal stability of $LiCoO_2$ cathode, J. Power Sources. 257 (2014) 286–292.

[47] H. Wang, Y.-I. Jang, B.Y. Huang, D. Sadoway, Y. Chiang, TEM Study of Electrochemical Cycling-Induced Damage and Disorder in $LiCoO_2$ Cathodes for Rechargeable Lithium Batteries, J. Electrochem. Soc. 146 (1999) 473–480.

[48] P. Yan, J. Zheng, M. Gu, J. Xiao, J.-G. Zhang, C.-M. Wang, Intragranular cracking as a critical barrier for high-voltage usage of layer-structured cathode for lithium-ion batteries, Nat. Commun. 8 (2017) 14101.

[49] C. Sun, K. Zhao, Y. He, J. Zheng, W. Xu, C. Zhang, X. Wang, M. Guo, L. Mai, C. Wang, M. Gu, Interconnected Vertically Stacked $2D\text{-}MoS_2$ for Ultrastable Cycling of Rechargeable Li-Ion Battery, ACS Appl. Mater. Interfaces. 11 (2019) 20762–20769.
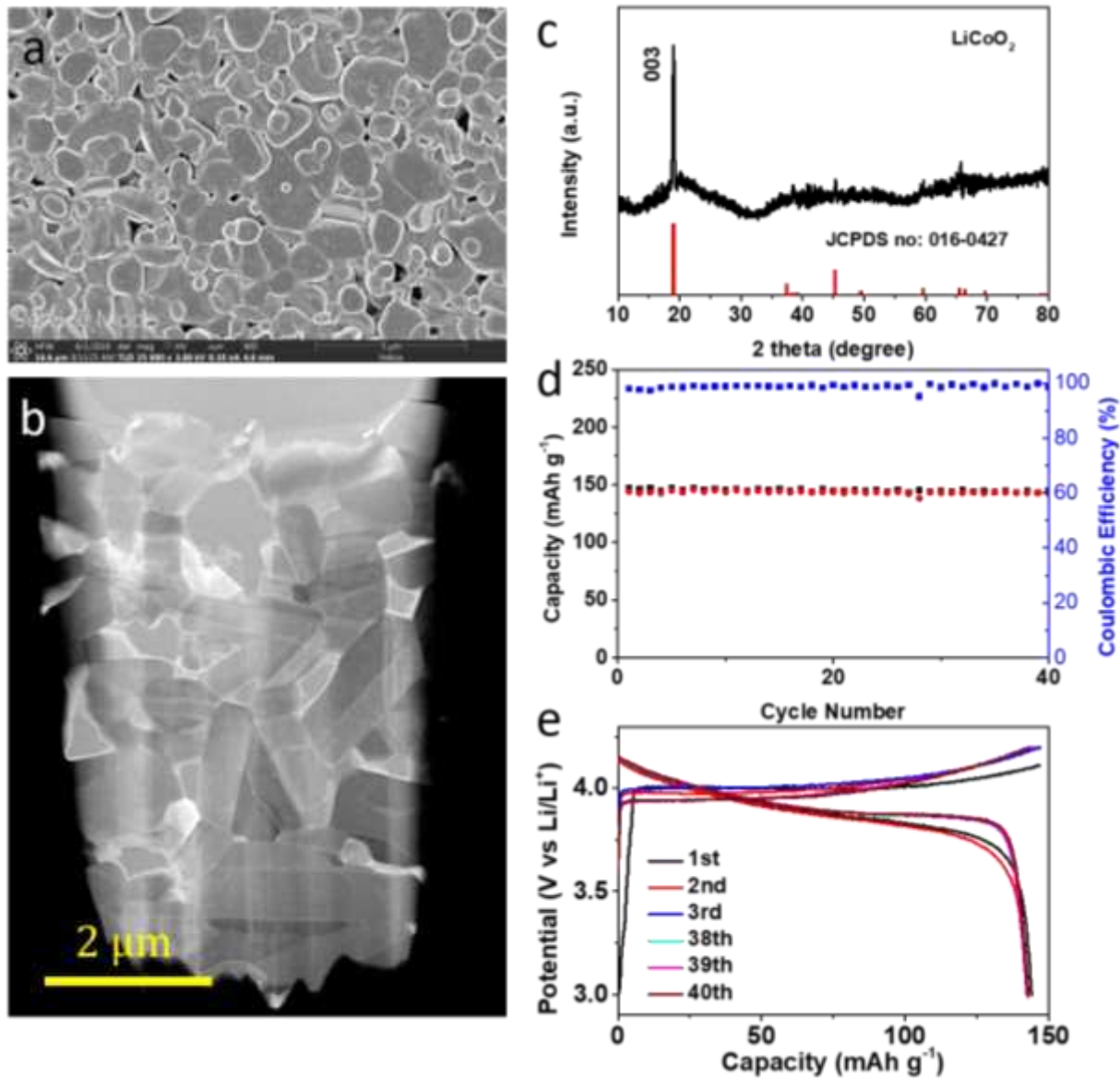
FIGURES

Fig. 1 Morphology and electrochemical performance of the LCO cathode. **a**, **b,** Top-down SEM and cross-section ABF-STEM images of the densely packed LCO crystals. **c**, XRD pattern of the LCO cathode, showing a perfect α-NaFeO₂ layered structure with R3̄m space group. **d**, Cycling performance of the LCO cathode. **e**, Charge and discharge curves of the LCO cathode.
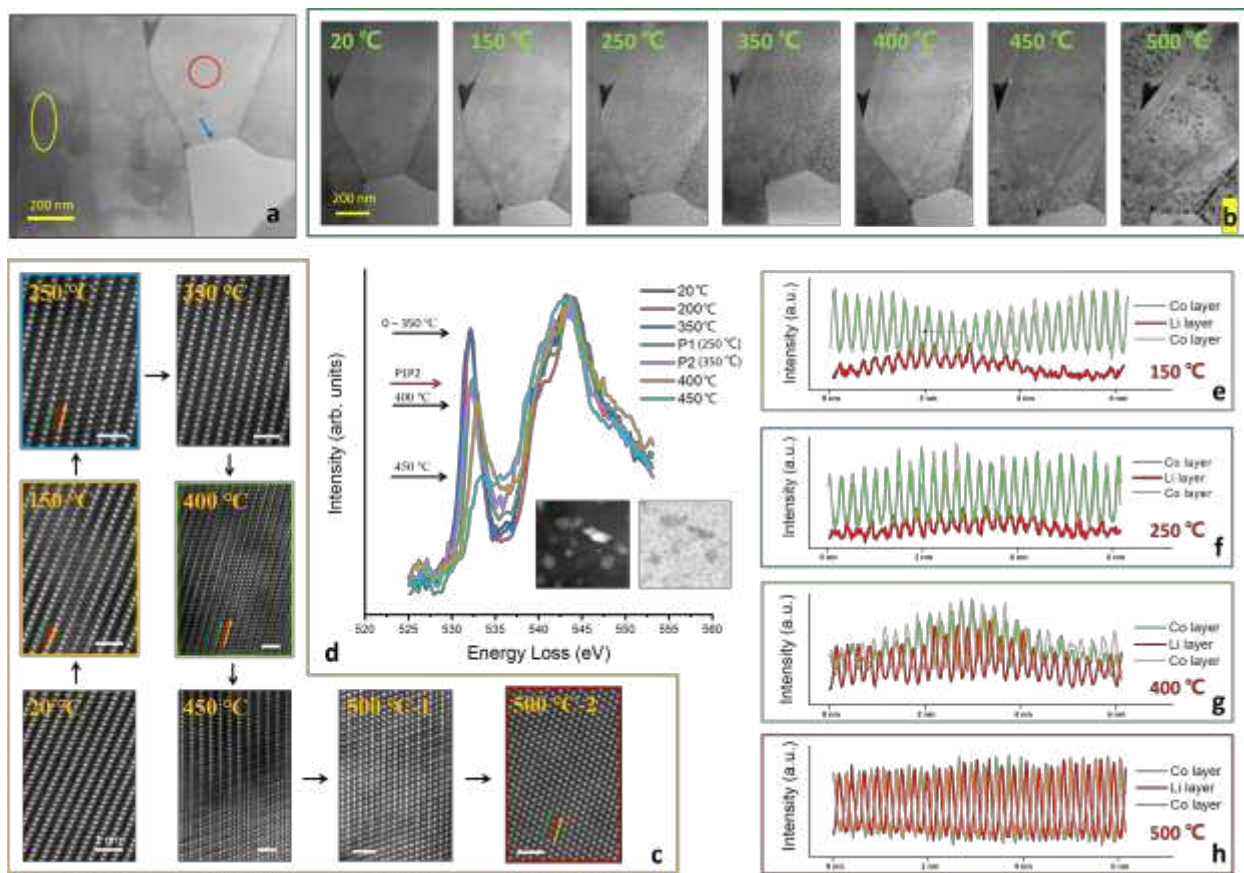
Fig. 2 Thermal behavior of the center LCO area. **a,** Low magnification HAADF-STEM image of three target areas of the LCO cathode. The red circle indicates the center thick area while the yellow ellipse indicates the thin edge area. The blue arrow is the boundary with different valence states. **b, c**, Low magnification and atomic resolution HAADF-STEM images of the center area as a function of temperature. **d**, Comparison of the O K-edge EELS. **e,** Intensity line profile along the green and red arrows indicated in **d**.
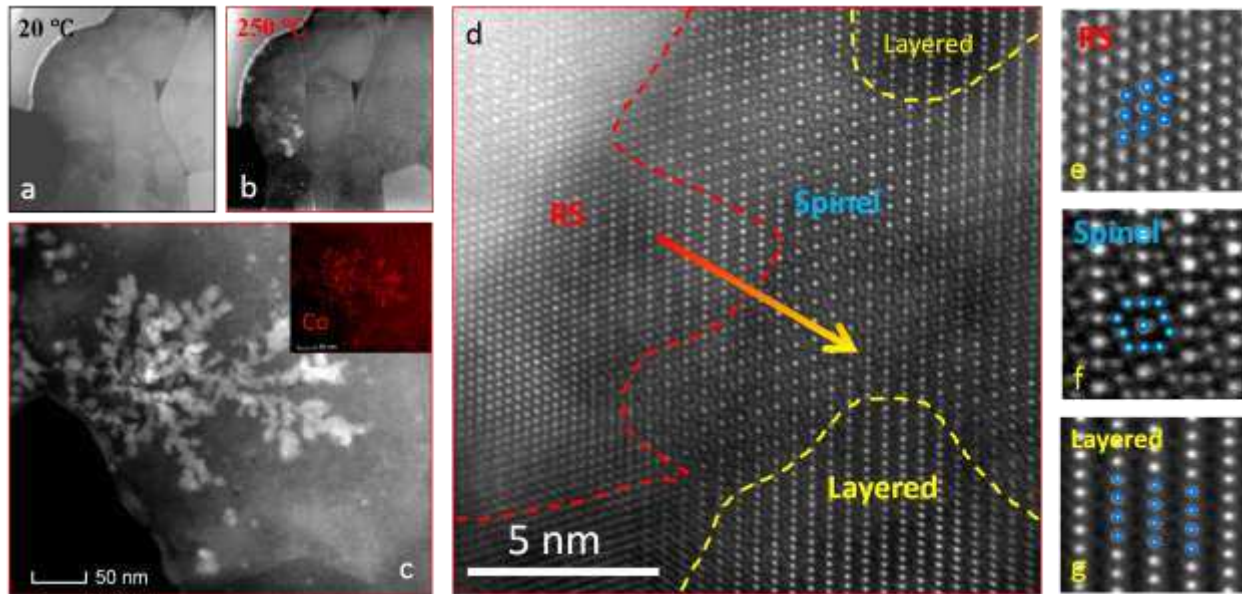
Fig. 3 Thermal behavior of the edge LCO area. **a, b,** Low magnification HAADF-STEM images at room temperature and at 250 ℃. **c**, EDS mapping of the dendrite phase showing a Co enrichment as it propagates. **d**, Atomic resolution HAADF-STEM image at the propagating front of the dendrite phase. **e-g**, Magnified images of the corresponding areas marked in **d**, projected atomic models are superimposed. Since only Co is visible in a HAADF-STEM image, the atomic model only contains the Co ions for better visualization.
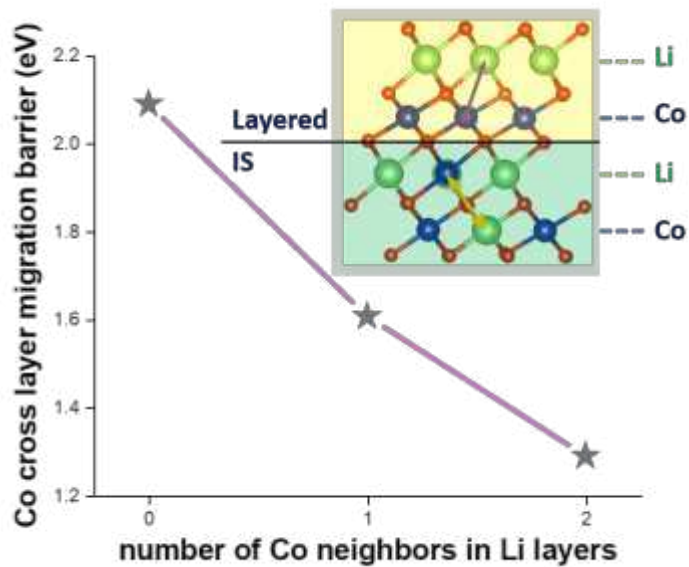
Fig. 4 Co diffusion barrier (purple arrow) in the layered phase as a function of the number of

Co-Li exchange (yellow arrow) in the IS phase. Data obtained from DFT calculations.
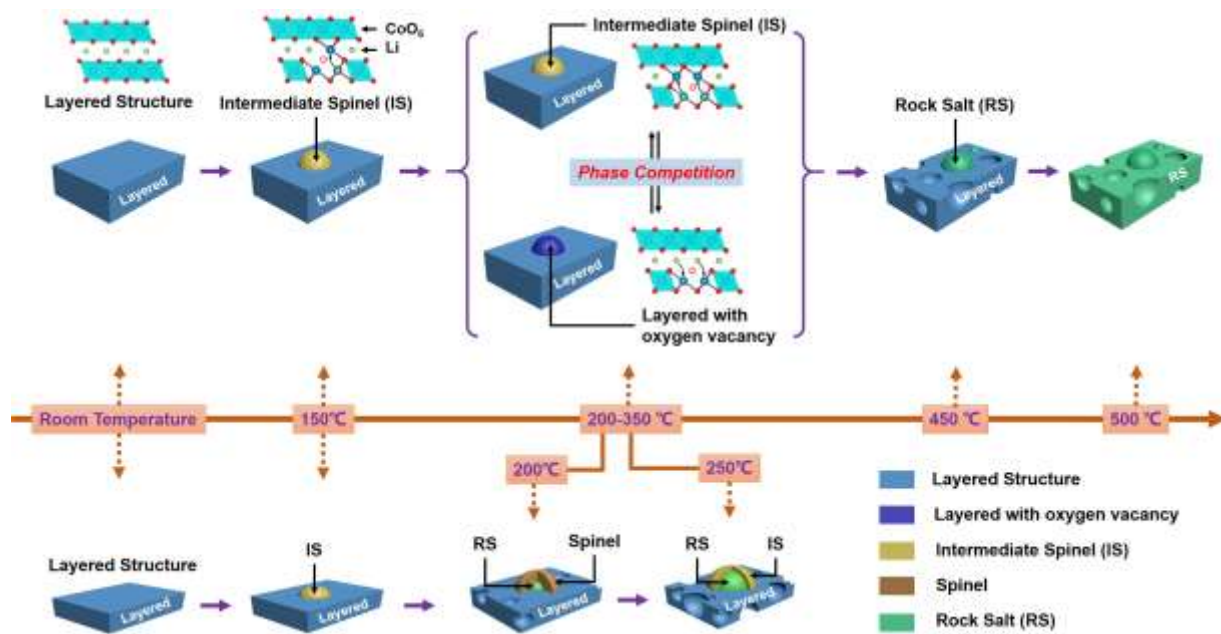

Fig. 5 Schematic illustration of the heterogenous thermal degradation of the center area (top)
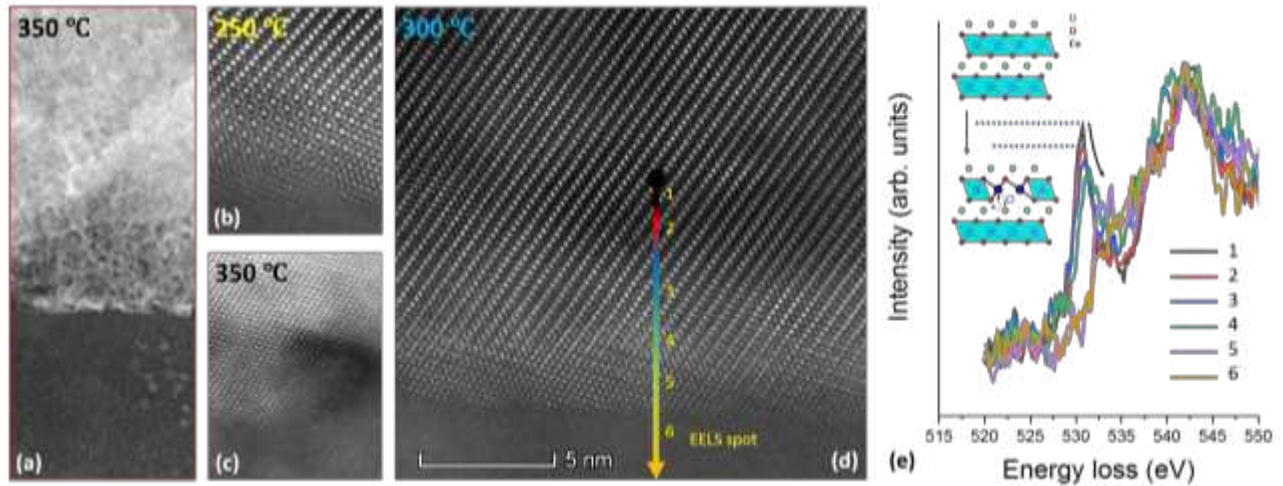
and the edge area (bottom) of the LCO cathode.

Fig. 6 Thermal behavior of the interparticle boundary with valence variation. a, LAADF-STEM image showing a strong strain contrast at the boundary. **b-d**, Atomic resolution HAADF-STEM image taken at different temperatures. **e**, Comparison of the O K-edge EELS at the locations marked 1 to 6 in **d**. The inset shows the formation of an oxygen vacancy and Co cross-layer migration.